

1-8-2019

A Contraction Stress Model of Hypertrophic Cardiomyopathy due to Sarcomere Mutations.

Rachel Cohn

The Jackson Laboratory, rachel.cohn@jax.org

Ketan Thakar

The Jackson Laboratory, ketan.thakar@jax.org

Andre Lowe

Feria A Ladha


The Jackson Laboratory, feria.ladha@jax.org

Anthony M Pettinato

The Jackson Laboratory, anthony.pettinato@jax.org

See next page for additional authors

Follow this and additional works at: <https://mouseion.jax.org/stfb2019>

 Part of the [Life Sciences Commons](#), and the [Medicine and Health Sciences Commons](#)

Recommended Citation

Cohn, Rachel; Thakar, Ketan; Lowe, Andre; Ladha, Feria A; Pettinato, Anthony M; Romano, Robert; Meredith, Emily; Chen, Yu-Sheng; Atamanuk, Katherine; Huey, Bryan D; and Hinson, J Travis, "A Contraction Stress Model of Hypertrophic Cardiomyopathy due to Sarcomere Mutations." (2019). *Faculty Research 2019*. 8.

<https://mouseion.jax.org/stfb2019/8>

This Article is brought to you for free and open access by the Faculty Research at The Mouseion at the JAXlibrary. It has been accepted for inclusion in Faculty Research 2019 by an authorized administrator of The Mouseion at the JAXlibrary. For more information, please contact ann.jordan@jax.org.

Authors

Rachel Cohn, Ketan Thakar, Andre Lowe, Fera A Ladha, Anthony M Pettinato, Robert Romano, Emily Meredith, Yu-Sheng Chen, Katherine Atamanuk, Bryan D Huey, and J Travis Hinson



A Contraction Stress Model of Hypertrophic Cardiomyopathy due to Sarcomere Mutations

Rachel Cohn,^{1,5} Ketan Thakar,^{1,5} Andre Lowe,¹ Ferial A. Ladha,^{1,2} Anthony M. Pettinato,^{1,2} Robert Romano,^{1,2} Emily Meredith,^{1,2} Yu-Sheng Chen,¹ Katherine Atamanuk,³ Bryan D. Huey,⁴ and J. Travis Hinson^{1,2,*}

¹The Jackson Laboratory for Genomic Medicine, 10 Discovery Drive, Farmington, CT 06032, USA

²University of Connecticut School of Medicine, 263 Farmington Avenue, Farmington, CT 06032, USA

³Department of Biomedical Engineering, University of Connecticut, Storrs, CT 06269, USA

⁴Department of Materials Science and Engineering, University of Connecticut, Storrs, CT 06269, USA

⁵Co-first author

*Correspondence: travis.hinson@jax.org

<https://doi.org/10.1016/j.stemcr.2018.11.015>

SUMMARY

Thick-filament sarcomere mutations are a common cause of hypertrophic cardiomyopathy (HCM), a disorder of heart muscle thickening associated with sudden cardiac death and heart failure, with unclear mechanisms. We engineered four isogenic induced pluripotent stem cell (iPSC) models of β -myosin heavy chain and myosin-binding protein C3 mutations, and studied iPSC-derived cardiomyocytes in cardiac microtissue assays that resemble cardiac architecture and biomechanics. All HCM mutations resulted in hypercontractility with prolonged relaxation kinetics in proportion to mutation pathogenicity, but not changes in calcium handling. RNA sequencing and expression studies of HCM models identified p53 activation, oxidative stress, and cytotoxicity induced by metabolic stress that can be reversed by p53 genetic ablation. Our findings implicate hypercontractility as a direct consequence of thick-filament mutations, irrespective of mutation localization, and the p53 pathway as a molecular marker of contraction stress and candidate therapeutic target for HCM patients.

INTRODUCTION

Hypertrophic cardiomyopathy (HCM) is a human disorder that affects 1 in 500 individuals with uncertain mechanisms (Maron et al., 1995). Patients with HCM are diagnosed by the presence of unexplained left ventricular hypertrophy (LVH) with preserved systolic contractile function (Ho et al., 2002). In young athletes, HCM manifests as a common cause of sudden cardiac death; while, in adults, HCM is associated with heart failure that may progress to require cardiac transplantation (Gersh et al., 2011b). Over the last few decades, the genetic basis of HCM has been demonstrated by inheritance of autosomal dominant mutations in components of the force-producing sarcomere (Maron et al., 2012). About two-thirds of HCM patients harbor heterozygous mutations in one of two sarcomere genes: myosin heavy chain β (MHC- β is encoded by *MYH7*) or myosin-binding protein C (cMyBP-C is encoded by *MYBPC3*) (Maron et al., 2012). Along with titin, MHC- β and cMyBP-C are located in the thick filament where ATP hydrolysis by MHC- β is coupled to force generation through interactions with the actin-rich thin filament (Figure 1A). A prevailing model suggests that HCM mutations alter cardiac force generation through dysregulation of calcium handling (Ashrafian et al., 2011; Lan et al., 2013). Whether *MYBPC3* and *MYH7* mutations result in HCM by shared or heterogeneous mechanisms remains undetermined.

Recent functional studies of thick-filament HCM mutations in reconstituted sarcomere and cardiomyocyte assays

have supported both gain- and loss-of-force production models of HCM pathogenesis, thus suggesting that changes in force production may not be a shared consequence of HCM mutations. For example, MYH7-R453C (arginine 453 substituted with cysteine) increased while MYH7-R403Q (arginine 403 substituted with glutamine) decreased force production in reconstituted actomyosin motility assays (Nag et al., 2015; Sommese et al., 2013). Equally puzzling, contractile studies of single cardiomyocytes from MYH6-R403Q^{+/-} mouse models, which recapitulate LVH and fibrosis *in vivo* (Geisterfer-Lowrance et al., 1990), have produced similarly conflicting results for the identical mouse model and strain (Chuan et al., 2012; Kim et al., 1999). Human patient-specific induced pluripotent stem cell (iPSC) HCM models of MYH7-R663H (arginine 663 substituted with histidine) have recapitulated some features of HCM including cellular enlargement and altered calcium handling (Lan et al., 2013), but mechanical phenotypes of HCM iPSC models have not been comprehensively studied.

The apparent difficulty in establishing the pathogenesis of HCM has been attributed in part to: (1) multiprotein assembly limitations that hinder sarcomere functional analysis, (2) mouse models that express distinct sarcomere components compared with humans (e.g., *MYH6* instead of *MYH7*), (3) the lack of isogenic iPSC-derived cardiomyocyte cell lines to control for genetic and epigenetic variation, and (4) the absence of biomimetic 3D human cardiac tissue functional assays. Here, we set out to address these limitations by combining genetic engineering tools to



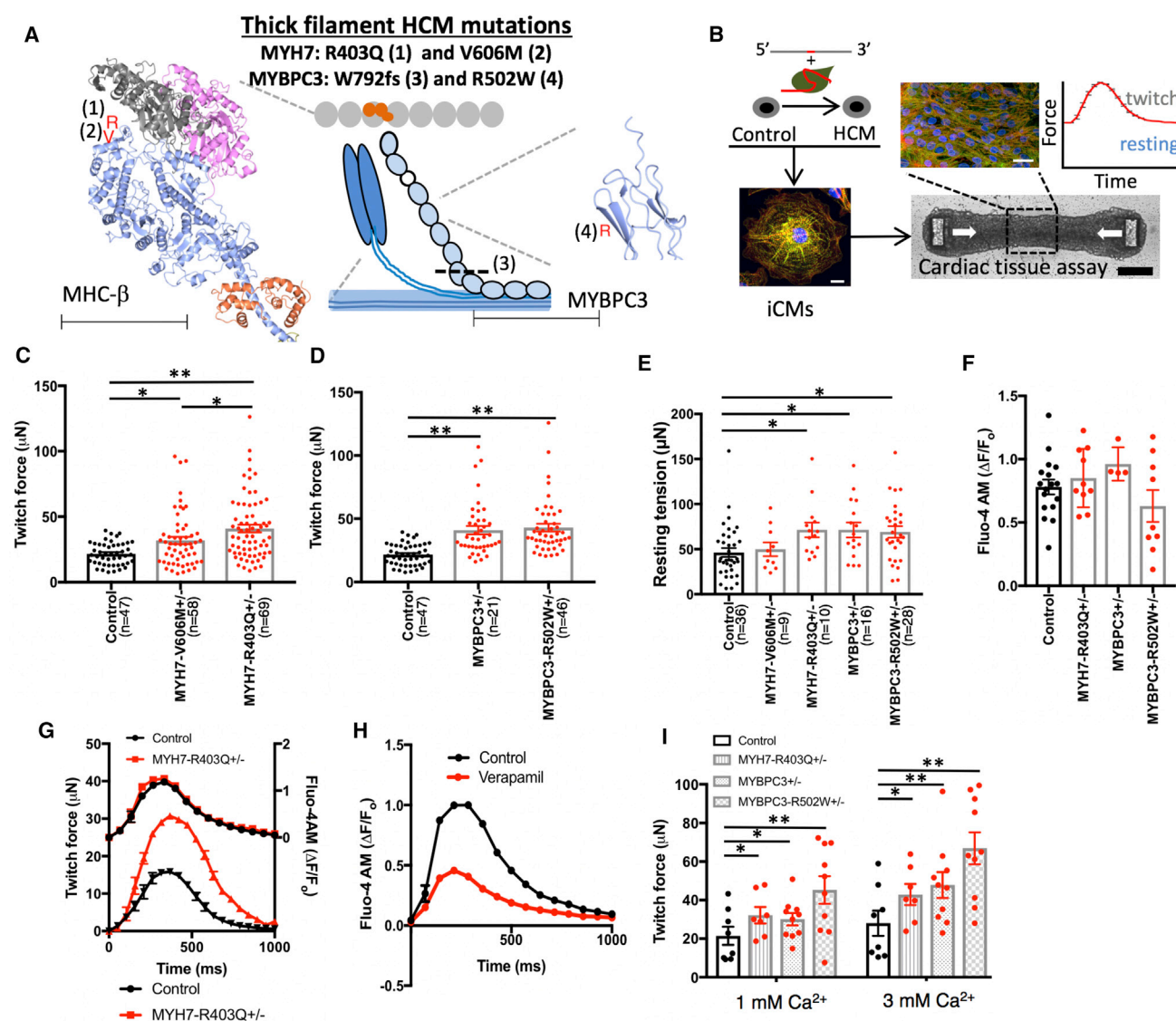


Figure 1. Human iPSC-Derived CMT Models with Thick-Filament HCM Mutations Result in Hypercontractility

(A) A representation of the sarcomere is shown that includes thick-filament components myosin heavy chain β (MHC- β) (blue globular heads connected to thin rods) and myosin-binding protein C (MYBPC3) (chain of light blue ovals); and thin-filament components actin (gray ovals) and the troponin complex (orange ovals). Location of mutations are decorated on the crystal structures of MHC- β -S1 (blue ribbon, left) and a domain of MYBPC3 (blue ribbon, right) (Fujii and Namba, 2017). Note: MHC- β -S1 is shown interacting with two actin molecules (gray and pink ribbons) and a regulatory light chain (orange ribbon). For MYH7, R403Q is identified by a red R (1), and V606M is denoted by a red V (2). For MYBPC3, the location of the truncation W792fs is denoted by a dashed line (3), and R502W is denoted by a red R (4). Scale bars, 62.5 \AA (MHC- β) and 31 \AA (MYBPC3).

(B) Experimental outline of isogenic HCM model generation using the guide RNA (gRNA)/Cas9 complex and single-stranded oligodeoxynucleotide to introduce HCM mutations into a control iPSC line. iPSCs are then differentiated to produce iCMs that are combined with fibroblasts and an extracellular matrix slurry for CMT production. Scale bar, 10 μ m. White arrows depict direction of contraction. Scale bars, 25 μ m (top panel) and 200 μ m (bottom panel). Both tissue twitch force and resting tension are quantified as well as CMT sarcomere structure by immunofluorescence.

(C) Maximum twitch force from CMTs generated from control, MYH7-V606M^{+/-} and MYH7-R403Q^{+/-} iCMs.

(D) Maximum twitch force from CMTs composed of control, MYBPC3^{+/-}, and MYBPC3-R502W^{+/-} iCMs.

(E) Resting tension produced by HCM CMTs compared with controls.

(F and G) Quantification of calcium transients ($\Delta F/F_0$) measured in HCM and control CMTs stained with Fluo-4 while pacing at 1 Hz (F). See representative tracing in (G).

(legend continued on next page)



generate a series of scarless *MYH7* and *MYBPC3* HCM mutations in human isogenic iPSCs that are differentiated to cardiomyocytes (iCMs) that express human sarcomere contractile components. We generated 3D cardiac microtissues (CMTs) (Figure 1B) to identify mechanical consequences of HCM mutations in combination with molecular assays to interrogate insights into HCM pathogenesis.

RESULTS

Generation of HCM iPSC and CMT Models Using CRISPR/Cas9

We began by identifying two HCM mutations in *MYH7*, R403Q and V606M (valine 606 substituted with methionine), which cause autosomal dominant HCM in both humans (Geisterfer-Lowrance et al., 1990; Marian et al., 1995) and mice (Blankenburg et al., 2014; Geisterfer-Lowrance et al., 1996). Both mutations are located in subfragment 1 (S1) of MHC- β near the actin-interacting domain (Figure 1A), but R403Q leads to a more severe cardiomyopathy compared with V606M (Blankenburg et al., 2014). Because MHC- β physically interacts with MYBPC3 (Maron et al., 2012), we hypothesized that these mutations could lead to HCM by a shared mechanism.

We next selected a common pathogenic truncation mutation in *MYBPC3* (clinvar.com), a guanine insertion that leads to tryptophan 792 substituted with valine followed by a frameshift (Trp792ValfsX41; MYBPC3^{+/-}), and a common pathogenic missense mutation, arginine 502 substituted with tryptophan (R502W) that is found in up to 2.4% of HCM patients (Figure 1A) (Saltzman et al., 2010). We generated scarless, isogenic iPSC models of these four mutations with CRISPR technology using delivery of a single optimized guide RNA, Cas9 nuclease, and a single-stranded oligodeoxynucleotide repair template (Figure 1B; Table S1). We chose an isogenic approach to focus our investigation on the direct functional consequences of the four thick-filament mutations, while controlling for background epigenetic and genetic variation. To generate the four iPSC models, we screened 1,111 clones by Sanger sequencing (Table S1). After screening for off-target genome-editing loci by sequencing (crispr.mit.edu) and karyotype abnormalities by virtual karyotyping using arrays (Table S2), we directly differentiated iPSCs (Lian et al., 2013) followed by metabolic enrichment (Tohyama et al., 2013) to generate purified iCMs. Finally, we combined iCMs with tissue-forming fibroblasts and an extracel-

lular matrix slurry to generate a 3D CMT assay that recapitulates native cardiac architecture and mechanics, which has been adapted from prior assays applied to study contractility phenotypes of dilated and PRKAG2 cardiomyopathy iPSC models (Boudou et al., 2012; Hinson et al., 2015, 2016).

Thick-Filament HCM Mutations Result in Hypercontractility

To study the mechanical consequences of *MYH7* and *MYBPC3* mutations in a biomimetic context, we first optimized our CMT assay (Hinson et al., 2015, 2016) to increase sarcomere gene expression of thick-filament transcripts. In particular, *MYH7:MYH6* is upregulated in the developing human heart (Wessels et al., 1991) and iCMs express fetal-to neonatal-stage transcript levels. By increasing the size of the microfabricated tissue gauges, including a proportional increase in cantilever dimensions and spring constant (Figure S1A), we improved CMT durability from 4 to 10 days (Figure S1B), which was associated with a 42% increase in *MYH7:MYH6* expression (Figure S1C, left panel) and 630% increase in cardiac troponin I (*TNNI3*) expression (Figure S1C, right panel). We utilized this improved CMT assay to study HCM mutations. For all CMT studies, we measured contractility parameters on day 7 after tissue compaction has completed and force production has plateaued (Figure S1D).

CMTs generated from iCMs with *MYH7*-R403Q^{+/-} (Figure S1E) generated a 40.9- μ N twitch force compared with 21.7 μ N in isogenic controls (Figure 1C). We then tested whether the increased twitch force generated by R403Q^{+/-} was secondary to changes in sarcomere isoform expression or clonal variation. *TNNI3* expression (Yang et al., 2014), a transcript marker that is related to cardiomyocyte maturation, was unchanged (Figures S2A and S2B) (Yang et al., 2014). Increased contraction force was also similar between two independent R403Q^{+/-} clones (Figure S2C). Moreover, CMT cross-sectional area did not differ between HCM mutations and isogenic controls (Figure S2D), which confirmed that HCM tissues were not hypercontractile secondary to increased CMT thickness. We next tested whether CMT assays could predict pathogenicity of *MYH7* mutations by testing CMTs generated from iCMs with the less-pathogenic *MYH7* variant V606M^{+/-}, which is also located in the actin-binding domain of S1 (Figure S1F). V606M^{+/-} CMTs generated a 31.9- μ N twitch force compared with 21.7 μ N in isogenic controls (Figure 1C), which was less than R403Q^{+/-}. We

(H) Representative calcium transient tracing of control iCMs treated with verapamil or carrier control.

(I) Dependence of maximum twitch force generated by HCM and control CMTs from extracellular calcium concentration.

Significance assessed by ANOVA (C-F and I) (*all $p < 0.05$ and **all $p < 0.001$); data are means \pm SEM (error bars) (C-I). Each data point represents a single CMT (C-F and I) generated by at least three biological replicates by iPSC differentiation batch.

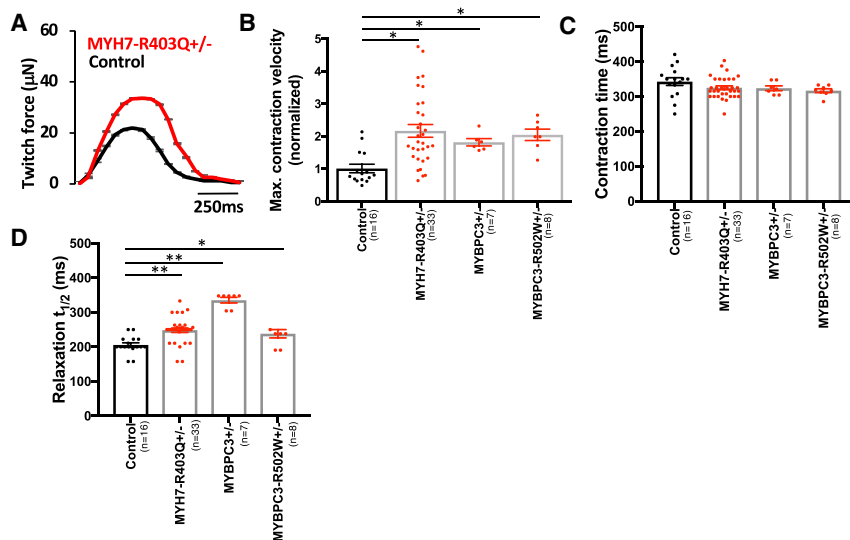


Figure 2. Contraction and Relaxation Kinetics Are Altered by HCM Mutations

(A) Representative twitch force tracings from MYH7-R403Q^{+/-} CMT models compared with isogenic controls.

(B–D) Normalized maximum contraction velocity (B), contraction time (C), and relaxation half-time (t_{1/2}) (D) for MYBPC3^{+/-}, MYBPC3-R502W^{+/-}, and MYH7-R403Q^{+/-} compared with controls.

Significance was assessed by ANOVA (B–D) (*all p < 0.05 and **all p < 0.001); data are means ± SEM (error bars) (A–D). Each data point represents a single CMT (B–D) generated by at least three biological replicates by iPSC differentiation batch.

concluded that *MYH7* variant pathogenicity positively correlates with maximum contraction force in CMT assays for the two mutations tested. We also generated two *MYBPC3* mutant CMT models to compare with *MYH7* models. MYBPC3^{+/-} and MYBPC3-R502W^{+/-} CMTs generated a 41.0- and 42.9-μN twitch force compared with 21.7 μN in isogenic controls, respectively (Figure 1D and Videos S1 and S2). Because sarcomere function also contributes to twitch-independent contraction force, or resting tension, we measured this parameter in CMTs. In parallel to twitch force changes, resting tension was increased in all HCM models except for MYH7-V606M^{+/-} (Figure 1E). Because V606M^{+/-} results in a mild phenotype, we did not further characterize this variant.

To characterize the molecular basis of HCM hypercontractility, we measured both calcium transients and levels in CMTs by optical imaging and calcium-dependent fluorescent dyes. HCM-associated hypercontractility was not related to changes in calcium delivery to the myofilament as calcium transients were unaffected in all HCM mutations tested (Figures 1F and 1G). This is distinct from CMT treatment with verapamil, a voltage-gated calcium channel blocker, which resulted in diminished CMT force production in parallel to reduced calcium transients as expected (Figure 1H). Because the increase in resting tension observed in HCM CMTs could be secondary to myofilament activation due to increased resting calcium levels, we stained iCMs with Indo-1 and measured both resting and caffeine-induced activation. Indo-1 signal was unchanged in HCM CMTs compared with controls at baseline and after caffeine treatment (Figures S2E and S2F). Finally, we tested CMT force production at low and high calcium concentrations (1 and 3 mM) to address the dependence of extracellular calcium on HCM hypercontractility. We

found that at both low (1 mM) and high (3 mM) calcium levels, HCM CMTs compared with controls resulted in hypercontractility (Figure 1I). These data support a model whereby thick-filament HCM mutations result in hypercontractility that is independent of variant localization, myofilament calcium delivery, and extracellular calcium levels.

We also measured HCM-associated contraction and relaxation kinetics by quantifying maximum contraction velocity, contraction time, and relaxation half-time across all HCM mutations. Compared with controls, HCM CMTs exhibited a 79%–121% increased maximum contraction velocity (Figures 2A and 2B), but without changes in contraction time (Figure 2C). Relaxation half-time (t_{1/2}) was prolonged (Figure 2D), which further supports that impaired relaxation is a consequence of HCM thick-filament mutations, which has also been documented in HCM patients (Ho et al., 2017). These kinetic changes are distinct from kinetic changes induced by omecamtiv mecarbil (Malik et al., 2011), a direct myosin activator that prolongs contraction time. We conclude that HCM mutations induce a state of hypercontractility that is distinct from how omecamtiv mecarbil activates MHC-β through stabilization of the lever arm (Planelles-Herrero et al., 2017).

Reduction of Hypercontractility by Calcium Channel Blockers and Direct Myosin Inhibitors

We generated CMTs from the severe HCM mutation MYH7-R403Q^{+/-}, and assessed changes in twitch force and resting tension after treatment with two candidate small molecules. We started by evaluating one of the most commonly prescribed therapies for HCM patients, the voltage-dependent L-type calcium channel blocker

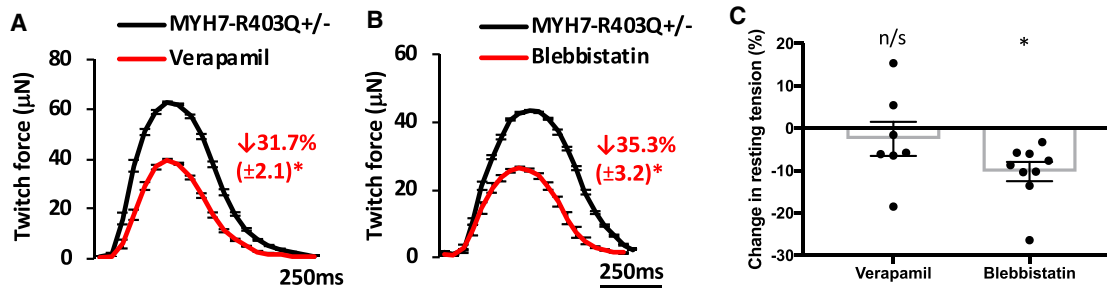


Figure 3. Reduction of Hypercontractility in MYH7-R403Q^{+/-} Tissues by Small Molecules

Representative tracings and percentage change in twitch force for MYH7-R403Q^{+/-} CMTs treated with carrier control (black tracing) compared with (A) verapamil (0.5 μM; red tracing) or (B) blebbistatin (10 μM; red tracing). (C) Comparison of the effects of verapamil and blebbistatin on resting tension in MYH7-R403Q^{+/-} CMTs. Significance was assessed by Student's t test (A–C) (*all $p < 0.05$); data are means \pm SEM (error bars) (A–C). Each data point represents a single CMT (C) generated by at least three biological replicates by iPS differentiation batch.

verapamil (Gersh et al., 2011a; Endoh and Blinks, 1988). In accord with changes in calcium transients (Figure 1H), the addition of verapamil reduced twitch tension by 31.7% in R403Q^{+/-} CMTs (Figure 3A). We also tested the direct myosin inhibitor blebbistatin to assess whether myosin inhibitors may similarly reduce HCM-associated hypercontractility in R403Q^{+/-} CMTs. Since blebbistatin binds to MHC- β distinct from residues near R403Q, and does not interfere with actin-binding or actomyosin disassociation (Kovacs et al., 2004), we hypothesized that this molecule may also reduce twitch force. Similar to verapamil, blebbistatin reduced twitch force by 35.3% (Figure 3B). Because blebbistatin inhibits myosin by a calcium-independent mechanism and resting calcium levels were not altered by HCM mutations, we hypothesized that only blebbistatin could normalize both twitch and resting tension induced by HCM mutations. Indeed, blebbistatin but not verapamil reduced resting tension by 10.2% (Figure 3C). These data obtained from R403Q^{+/-} CMTs suggest that therapeutic agents that reduce both twitch and resting forces may be more efficacious for HCM patients, which may explain why verapamil has limited clinical efficacy in HCM patients (Sen-Chowdhry et al., 2016).

MYH7-R403Q^{+/-} CMTs Exhibit Myofibrillar Disarray and iCM Hypertrophy

To determine whether HCM mutations affect sarcomere structure in CMTs, we fixed CMTs and stained sarcomeres using antibodies to Z-disc protein alpha actinin with DAPI co-stain (Figure 4A). We again focused on R403Q^{+/-} because this mutation is highly pathogenic in humans and in our mechanical assays. Z disk analysis of R403Q^{+/-} tissues demonstrated increased Z disk angular dispersion (Figures 4B and S3A), which is a measure of Z disk disarray. This result is consistent with myofibrillar disarray observed in HCM patients (Bulkley et al., 1977). Sarcomere length

and cell number were not different (Figures S3B and S3C) in R403Q^{+/-} CMTs compared with isogenic controls. To assess iCM size, we fixed and immunostained R403Q^{+/-} iCMs (Figure 4C) because the analysis of individual iCMs is not feasible within our CMT assays. Single R403Q^{+/-} iCMs demonstrated increased iCM cell area (Figure 4D). We next measured levels of candidate hypertrophy signaling pathways including mitogen-activated protein kinase pathways, AKT and CAMKII, as these have been implicated in cardiomyocyte hypertrophy *in vivo* and in iCMs (Hinson et al., 2015; Zhang et al., 2003). In proportion to increased iCM cell area, lysates from R403Q^{+/-} iCMs had elevated levels of phosphorylated ERK2 and AKT (Figures 4E–4G), but not p38, JNK, or CAMKII (Figure S3D). In summary, R403Q^{+/-} mutations result in sarcomere disorganization in CMT assays, and iCM hypertrophy in parallel with increased ERK2 and AKT signaling.

RNA Sequencing Identifies Activation of p53 Signaling in HCM Models

To identify molecular mechanisms of HCM mutations, we applied RNA sequencing to iCM samples from HCM mutations (MYH7-R403Q^{+/-}, MYBPC3^{+/-}, and MYBPC3-R502W^{+/-}) and compared the results with isogenic controls. We started by analyzing the MYBPC3^{+/-} mutation, tryptophan-792-valine-fs, to determine how MYBPC3 truncation mutations cause HCM. Consistent with nonsense-mediated messenger RNA decay, transcripts from the tryptophan-792-valine-fs allele were nearly absent compared with wild-type transcripts (Figure 5A). This is in contrast to the missense mutation R502W, which had no evidence of degradation of mutant transcripts. In parallel to changes in MYBPC3 transcript level, cMyBP-C protein content was also reduced in MYBPC3^{+/-} (Figures 5B and 5C) but not R502W^{+/-} (Figures S4A and S4B) by immunoblotting iCM lysates with an antibody that recognizes the

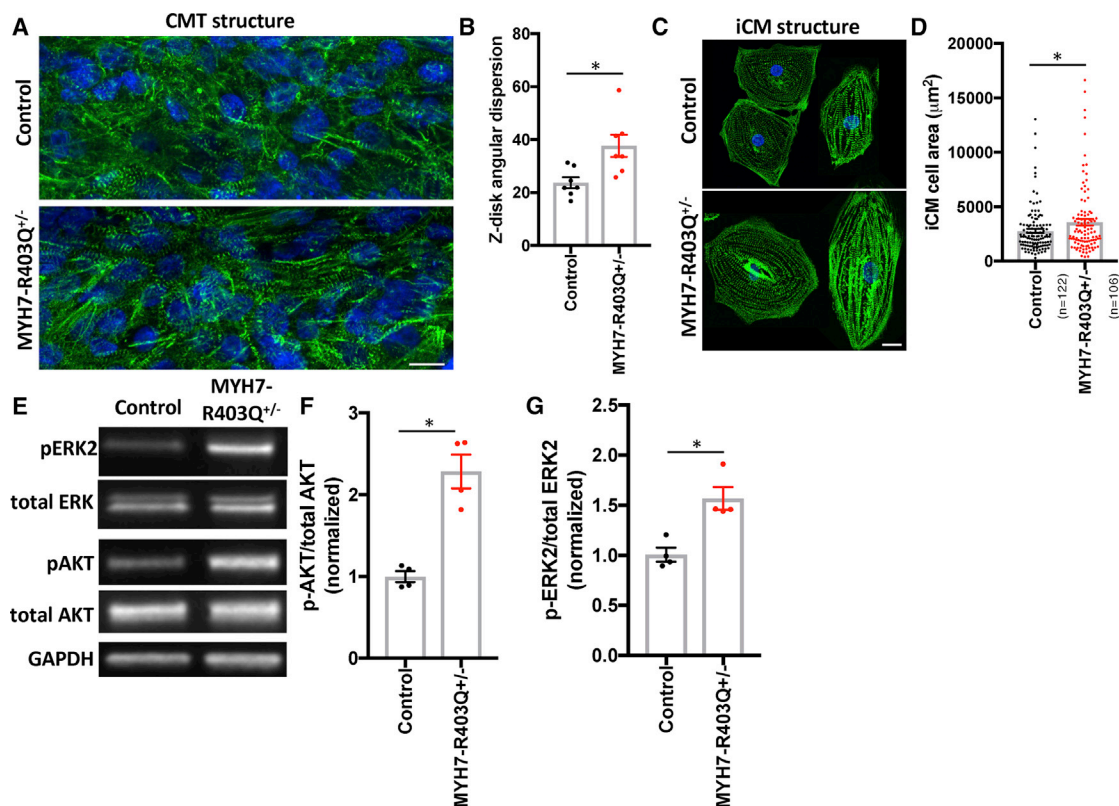


Figure 4. CMT and iCM Structural and Molecular Signaling Changes in MYH7-R403Q^{+/-} Models

(A) Representative confocal image of CMTs generated from MYH7-R403Q^{+/-} and control iCMs and decorated with antibodies to cardiac alpha actinin (green) and co-stained with DAPI (blue). Scale bar, 10 μm.

(B) Quantification of sarcomeric Z disk angular dispersion obtained from analysis of confocal regions of interest from CMTs decorated with antibodies to alpha actinin.

(C) Representative confocal images of single MYH7-R403Q^{+/-} and control iCMs decorated with antibodies to cardiac alpha actinin (green) and co-stained with DAPI (blue). Scale bar, 10 μm.

(D) Quantification of MYH7-R403Q^{+/-} and control iCM cell area from confocal images stained with alpha actinin.

(E–G) Representative immunoblots from MYH7-R403Q^{+/-} and control iCM lysates probed with antibodies to phospho- and total ERK (note: ERK2 is highly phosphorylated in iCM lysates) and phospho- and total AKT as well as GAPDH (loading control) (E). Normalized quantification of (F) phospho-AKT to total AKT and (G) phospho-ERK2 to total ERK2.

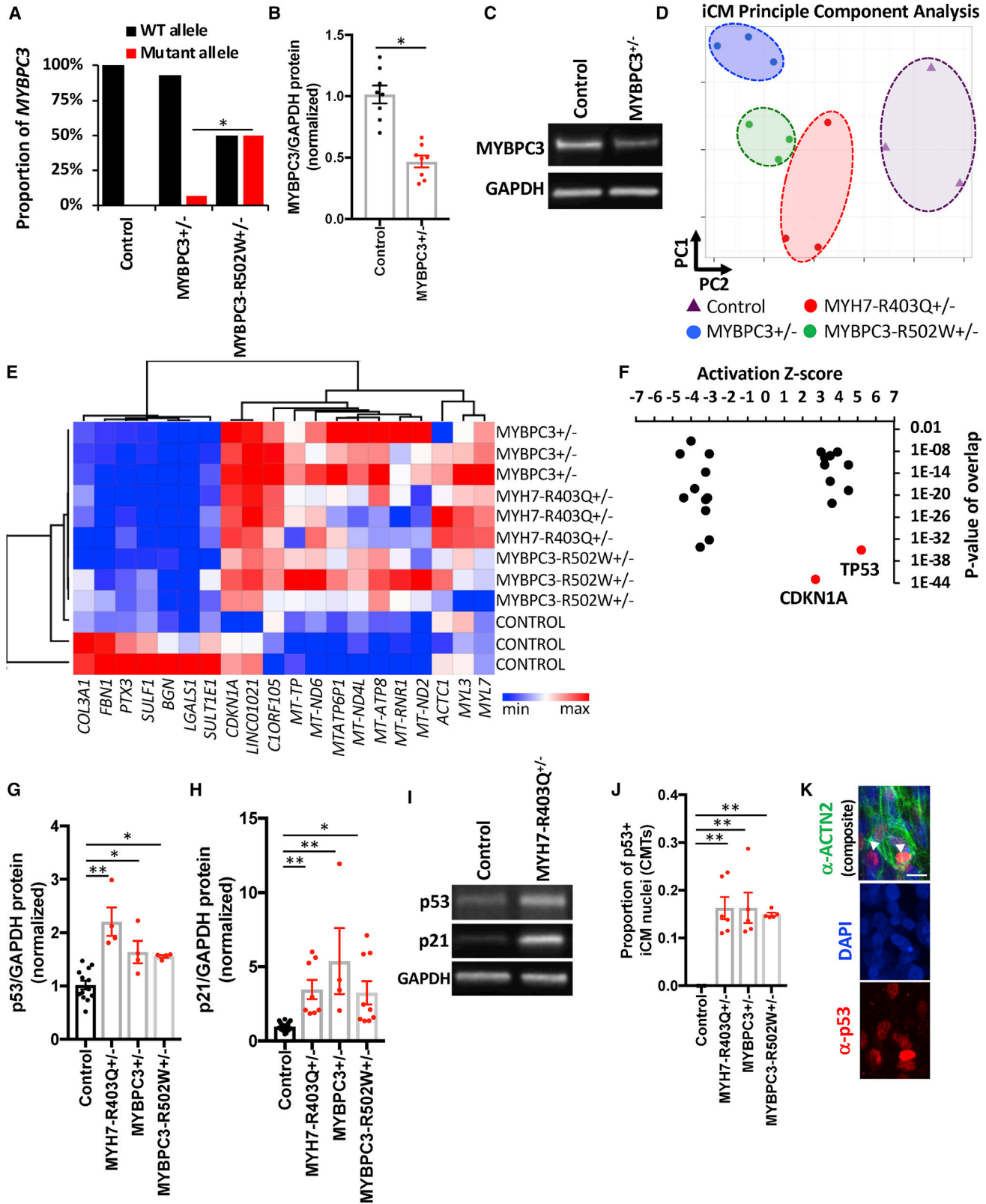
Significance was assessed by Student's t test (B, D, F, and G) (*all $p < 0.05$); data are means ± SEM (error bars) (B, D, F, and G). Each data point represents a single CMT (B), iCM (D), or sample generated from a batch of iCMs (F and G) generated by at least three biological replicates by iPS differentiation batch.

amino terminus of cMyBP-C proximal to the frameshift mutation. These data support a haploinsufficiency model of HCM-associated MYBPC3 frameshift mutations, and also that R502W is likely a loss-of-function missense mutation.

Next, we analyzed iCM gene transcripts by unsupervised principal-component analysis (PCA) to assess sample-to-sample distances. All HCM samples clustered distinctly from isogenic controls, while biological replicates within the same genotype clustered closely (Figures 5D and 5E; Table S3). Of note, gene components obtained from PC1 and PC2 include mitochondrial-encoded transcripts (*MT-TP*, *MT-ND6*, *MTATP6P1*, *MT-ND4L*, *MT-ATP8*, *MT-RNR1*,

and *MT-ND2*), extracellular matrix-related transcripts (*COL3A1*, *FBN1*, *SULF1*, *BGN*, and *LGALS1*), sarcomere transcripts (*ACTC1*, *MYL3*, and *MYL7*), and p53-related gene targets (*CDKN1A* and *LINC01021*) (Hunten et al., 2015).

To better define the HCM-associated gene transcript program, we analyzed differentially expressed transcripts that were common to all HCM iCM models (Figure S4C; Table S4). In accord with the close proximity of HCM samples by PCA analysis, differentially expressed transcripts were also highly shared among HCM models. Of 1,050 total up-regulated transcripts, 320 were shared by at least two HCM models, and of the 1,177 total downregulated transcripts,



(legend on next page)



419 were shared by at least two HCM models. Of note, the HCM phenotype did not correlate with expression of cardiac chamber-specific markers such as myosin light chain 7 (*MYL7*), myosin light chain 2 (*MYL2*), and potassium channel *HCN4* (Figure S4D). We then used differential expression results to perform pathway analysis in HCM iCM models using Ingenuity Pathway Analysis. Both p53 and CDKN1A (p21) pathways were predicted to be highly activated in HCM iCMs (Figure 5F; Table S5) as prioritized by activation Z score and p value of overlap. In parallel to transcript levels, p53 and p21 protein levels were increased in HCM iCM lysates (Figures 5G–5I). In addition, fixed and immunostained HCM CMTs also exhibited increased p53 staining within the nuclei of ACTN2+ iCMs (Figures 5J and 5K). Unexpectedly, these results implicate altered p53 signaling as a common molecular consequence of thick-filament HCM mutations.

HCM iCMs Exhibit a p53-Dependent Cytotoxicity Induced by Metabolic Stress

To understand the role of elevated p53 signaling in HCM iCM models, we first determined whether p53 activation reflected increased iCM stress. We started by re-examining RNA sequencing data for p53-dependent gene expression changes that function in the regulation of cell death including *BBC3*, *BAX*, and *FAS*. HCM iCMs have increased expression of these transcripts relative to controls (Han et al., 2001). We then tested whether HCM mutations resulted in increased iCM death in normal growth conditions (Figure S4E). We could identify no baseline change in iCM death, which was also consistent with our observation that CMT cell number and tissue cross-sectional area were not altered by HCM mutations. We then considered whether

HCM iCMs may be more susceptible to cell stress. Informed by the clinical observation that HCM patients have bio-energetic deficits *in vivo* (Crilly et al., 2003), as well as the increased expression of mitochondrial gene transcripts in HCM iCMs (Figure 5E), we measured iCM cell death induced by metabolic stress from glucose removal that has been used by others to induce energy stress (Jones et al., 2005). We found that HCM iCMs exhibited elevated cytotoxicity (Figure 6A) compared with controls, which was associated with increased ADP:ATP (Figure 6B)—a marker of metabolic stress. We next tested whether p53 knockdown by lentiCRISPR could rescue HCM-associated cytotoxicity induced by metabolic stress. P53 knockdown partially rescued HCM cytotoxicity induced by metabolic stress (Figure 6C), and also resulted in reduced expression of p53-target CDKN1A (Figure 6D).

To gain insights into molecular linkages between thick-filament HCM mutations and p53 activation, we started by measuring known regulators of p53, including DNA damage (Lakin and Jackson, 1999) and oxidative stress (Hwang et al., 2001). While the levels of phosphorylated histone 2A member X (Figure 6E), a marker of DNA damage was not different between R403Q^{+/-} iCMs compared with controls, reactive oxygen species (ROS) levels were increased over 3-fold (Figure 6F). Because ROS generation is generated by respiring mitochondria, we also stained iCMs with MitoSOX (Figure 6G) and MitoTracker dyes (Figure 6H) to quantify both mitochondrial-derived ROS and mitochondrial content, respectively. Compared with controls, HCM iCMs had higher mitochondrial-derived ROS production and mitochondrial content. Finally, we tested whether ROS inhibition by n-acetylcysteine (NAC) or p53 inhibition by pifithrin- α could normalize CMT force

Figure 5. RNA Sequencing of HCM and Isogenic Control iCMs

(A) By allele-specific analysis of gene transcripts obtained from isogenic control, MYBPC3^{+/-}, and MYBPC3-R502W^{+/-} iCMs; MYBPC3 transcripts were quantified for control (wild-type [WT]; black bar) and mutant (red bar) alleles and shown as the proportion of total MYBPC3 expression.

(B) Densitometry of immunoblots from protein lysates derived from control and MYBPC3^{+/-} iCMs, and probed for MYBPC3 (note: truncated MYBPC3 was not identified) and for protein loading with GAPDH.

(C) Representative immunoblot from (B).

(D) Principal-component analysis (PCA) of RNA transcripts from three biological replicates of isogenic control (purple triangles) and MYBPC3^{+/-} (blue circles), MYBPC3-R502W^{+/-} (green circles), and MYH7-R403Q^{+/-} iCMs (red circles).

(E) Hierarchical clustering of genes contributing to PC1 and PC2 from (D) and illustrated by heatmap (Table S2).

(F) Differentially expressed gene transcripts ($\log_2FC > 0.3$ or < -0.3 and false discovery rate < 0.1) were analyzed by pathway analysis using Ingenuity Pathway Analysis and identified pathways (black and red dots) were organized by activation Z score and p value of overlap.

(G–I) Densitometry of immunoblots from control and HCM iCM protein lysates, normalized for protein loading (GAPDH) (G) and probed with antibodies to p53 or (H) p21. See representative blots in (I).

(J and K) Quantification of iCM p53+ nuclei from confocal images of fixed CMTs immunostained with an antibody to p53 (red), cardiomyocyte-specific ACTN2, and DAPI co-stain (J). See representative image in (K), arrowhead marks p53+ nuclei that co-stain with ACTN2. Scale bar, 15 μ m.

Significance (* $p < 0.05$ and ** $p < 0.001$) was assessed by Fisher's exact test (A), Student's t test (B), or ANOVA (G, H, and J); and data are means \pm SEM (error bars) (B, G, H, and J). Each data point represents a sample generated from a batch of iCMs (B, D, E, G, and H) or single CMT (J) generated by at least three biological replicates by iPS differentiation batch.

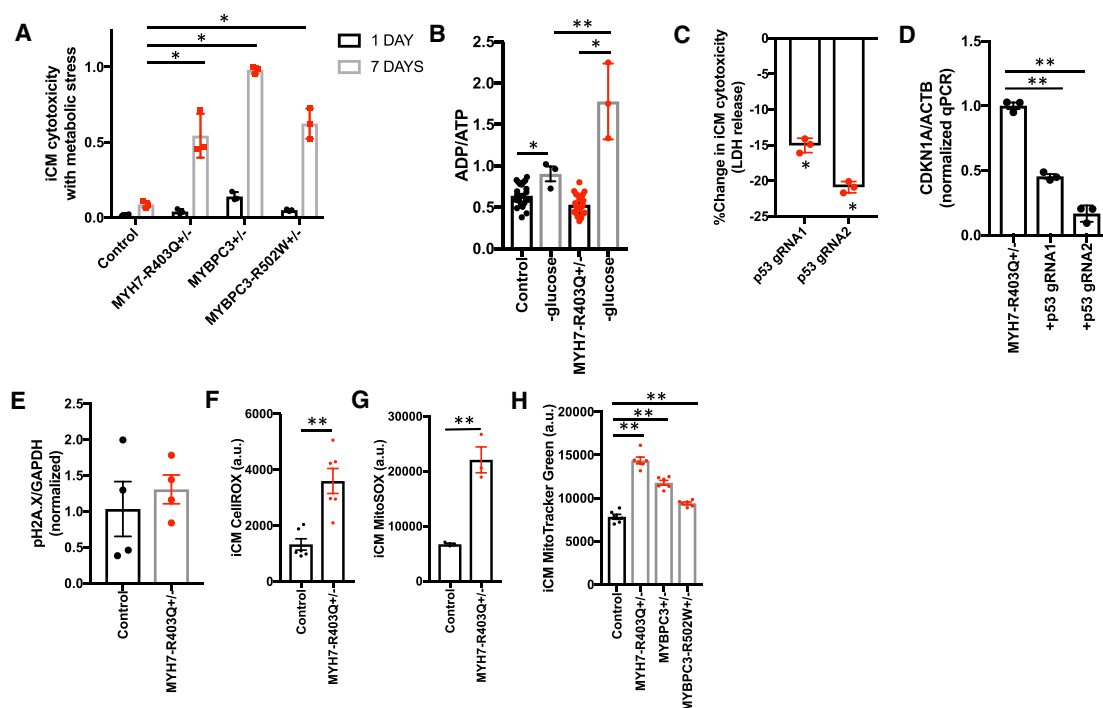


Figure 6. HCM iCMs Exhibit a p53-Dependent Cytotoxicity with Metabolic Stress that Is Related to Increased Oxidative Stress

(A) Proportion of iCM death after 1 and 7 days of metabolic stress induced by growth in glucose-free medium.

(B) ADP:ATP for iCMs cultured in normal growth medium and after 24 hr in glucose-free medium.

(C) Change in iCM cytotoxicity measured by lactate dehydrogenase (LDH) release assay upon p53 genetic knockdown using lentiCRISPR encoding two independent gRNAs that target the *TP53* gene.

(D) qPCR analysis of *CDKN1A* normalized to *ACTB* obtained from cDNA libraries generated from MYH7-R403Q^{+/-} iCMs transduced with lentiCRISPR encoding two independent *TP53* or non-targeted gRNAs.

(E) Quantification of phosphorylated H2A.X normalized to GAPDH using densitometry analysis of immunoblots from iCM lysates.

(F and G) Quantification of fluorescence (arbitrary units) using FACS analysis of iCMs stained with CellROX green (F) or MitoSOX red (G), a mitochondrial-specific probe for reactive oxygen species.

(H) Quantification of fluorescence (arbitrary units) using FACS analysis of iCMs stained with MitoTracker green.

Significance (* $p < 0.05$ and ** $p < 0.001$) was assessed by ANOVA (A) or Student's *t* test (B–H); and data are means \pm SEM (error bars) (A–H). Each data point represents results obtained from a sample generated from a batch of iCMs (A–H) generated by at least three biological replicates by iPS differentiation batch.

production in HCM CMTs. While pifithrin- α treatment had no influence on CMT twitch force, NAC treatment increased twitch force similarly in HCM and control CMTs. These data support that thick-filament HCM mutations result in hypercontractility independent from p53 activation and ROS production, and ROS is a negative regulator of CMT twitch force. In summary, we conclude that HCM mutations result in a state of contraction stress characterized by oxidative stress, p53 activation, and increased p53-dependent cytotoxicity in the setting of metabolic stress.

DISCUSSION

The genetic basis of HCM, most commonly due to thick-filament sarcomere mutations, was identified decades

ago, yet the mechanisms that link sarcomere gene mutations with the HCM phenotype still remain unclear, in part because of the lack of a robust human *in vitro* model system to interrogate HCM pathogenesis. Here, we engineered four human HCM models using CRISPR to generate isogenic mutations in two of the most commonly mutated sarcomere genes, and measured the mechanical and molecular consequences of these variants in a biomimetic CMT assay. We sought to determine the role of genetic heterogeneity on phenotypes identified in CMT and iCM functional assays. Our study demonstrated a convergent model of HCM pathogenesis whereby four thick-filament HCM mutations, irrespective of mutation localization, induced a state of hypercontractility due to both increased twitch and resting tensions in parallel with delayed relaxation kinetics. The increased resting tension has particular



importance as this component of sarcomere contraction is not affected by therapeutics that target only voltage-dependent factors, such as the L-type calcium channel, which are in clinical use for HCM patients, and provides a rationale for the identification of therapeutics such as direct myosin inhibitors that can reduce both resting and twitch contraction forces.

Our results of hypercontractility are in accord with recent functional studies of HCM-associated thin-filament mutant mouse models that support a sarcomere tension model (Davis et al., 2016). HCM mutations in thin-filament genes were found to increase tension primarily by increasing myofilament calcium sensitivity, as would be expected by changes in troponin complex function, while our findings are consistent with a model whereby thick-filament HCM mutations result in hypercontractility due to intrinsic changes in sarcomere function independent of changes in calcium delivery to the myofilament, and at least in part independent from changes in myofilament calcium sensitivity. Because thick-filament HCM mutations consistently increased iCM size, our study cannot exclude the contribution of iCM hypertrophy to hypercontractility, especially in relation to myofilament calcium sensitivity studies. Nonetheless, our model is also supported by recent biophysical studies of MHC- β and cMyBP-C interactions that report changes in the accessibility of myosin heads to generate force in the setting of HCM mutations (Nag et al., 2017). Our inability to observe previously described alterations in calcium handling may be due to the nature of the variants studied, non-cell-intrinsic mechanisms, or may be limited by the maturity state of all iCM studies. We propose that the calcium handling defects identified in other HCM studies are likely indirect consequences of sarcomere mutations such as induced by heart failure. In the future, it will be important to test other thick-filament variants to identify potential functional heterogeneity, as well as for comparison with thin-filament CMT phenotypes.

Our study illuminates how HCM-associated hypercontractility is maladaptive because it results in oxidative stress, which is associated with reduced iCM viability in the setting of metabolic stress *in vitro*. Energy imbalance in HCM patients with significant LVH has been identified in other studies (Jung et al., 1998), but to our knowledge our study is the first to implicate an early, cell-intrinsic metabolic vulnerability that results in altered cell survival. While we did not observe an energy imbalance in HCM iCMs in unstressed conditions, this may be secondary to the fetal nature of iCM metabolism that favors glucose rather than fatty acids for energy production. Our study also provides a new *in vitro* assay for screening therapeutics that modify HCM-associated iCM viability defects induced by metabolic stress, such as through genetic and chemical

screens, which may provide new therapeutic targets for HCM patients. Finally, we identify that HCM mutations result in increased p53 signaling. While, to our knowledge, p53 has been well studied in the context of cancer and other disorders, it has not been implicated in HCM pathogenesis and only recently implicated in regulating the cardiac transcriptome (Mak et al., 2017). Notably, p53 genetic ablation also protected against heart failure due to pressure overload, but promoted age-associated cardiac dysfunction (Mak et al., 2017). Our results suggest that p53 ablation would be beneficial in HCM, and therefore molecular linkages between sarcomere variants, oxidative stress, and p53 activation, will need to be addressed in future studies with potential therapeutic implications. Finally, our robust genome-engineered platform using isogenic human iPSCs combined with CMT assays demonstrates a robust approach to interrogate HCM pathogenesis, test cardiomyopathy therapeutics, as well as classify sarcomere gene variants of unknown significance.

EXPERIMENTAL PROCEDURES

iPSC Culture, iCM Differentiation, and Enrichment

The parental human iPSC line used for all studies was PGP1, a normal control line obtained from the Coriell Institute (GM23338) that has been described previously (Hinson et al., 2015, 2016). This study was approved by the Jackson Laboratory institutional review committee and institutional review board approval was obtained as part of the Personal Genome Project. All iPSC lines were maintained on Matrigel (Corning)-coated tissue culture plates in mTeSR1 medium (STEMCELL). iPSC lines were screened for copy-number variants using Illumina SNP arrays as described previously (Hinson et al., 2015). iPSCs were differentiated to iCMs by sequential targeting of the WNT pathway as described previously (Lian et al., 2013). iCMs were maintained in RPMI with B27 supplement (Thermo Fisher Scientific) unless otherwise noted. iCMs were enriched by metabolic selection by previously described methods (Tohyama et al., 2013). On day 12 of iCM differentiation, beating iCMs were enriched by adding 4 mM DL-lactate (Sigma) in glucose-free DMEM medium (Thermo Fisher Scientific) for 48 hr. Following selection, enriched iCMs were maintained in RPMI with B27 supplement. Only differentiation batches with >90% troponin T2+ cells by fluorescence-activated cell sorting (FACS) or estimated by morphology were considered to be high purity for further assays. For all assays, iCMs were studied on differentiation days 30–35. For all iCM and CMT assays, at least biological triplicates (differentiation batches) were studied.

CRISPR/Cas9 iPSC and iCM Gene Editing

Genetic modifications were generated using scarless iPSC clonal selection by following protocols described previously (Hinson et al., 2015). For MYH7 and MYBPC3 mutation generation, PGP1 iPSCs were electroporated with pCAG-eGFP-2A-CAS9 plasmid (obtained from Addgene), a single-stranded mutation-specific 90mer



oligonucleotide and an optimized guide RNA plasmid (Table S1). After 48 hr, GFP+ iPSCs were sorted by flow cytometry FACS, clonally expanded, and Sanger sequenced for genotyping. Guide RNAs were designed and optimized using *in silico* methods that reduce risk of off-target mutations (crispr.mit.edu). For *MYH7* R403Q gene editing, the corresponding region of *MYH6* was sequenced to verify no off-target *MYH6* mutation. For lentiCRISPR (v2) experiments (Addgene), protocols for guide RNA cloning and lentivirus production were obtained from published methods, and a multiplicity of infection of 3 was used (Sanjana et al., 2014).

CMT Production and Force Measurements

CMTs were prepared as described previously (Hinson et al., 2015). Polydimethylsiloxane (PDMS) (Sylgard 184 from Corning) cantilever devices were molded from SU-8 masters, with embedded 1- μ M fluorescent microbeads (carboxylate FluoSpheres; Thermo Fisher Scientific). PDMS tissue gauge substrates were treated with 0.2% pluronic F127 (Sigma) for 30 min to reduce cell-extracellular matrix interactions. iCMs were disassociated using trypsin digestion and mixed with stromal cells (human cardiac fibroblasts; single lot obtained from Lonza), which were pre-treated with 10 μ g/mL mitomycin C (Sigma) to prevent cell proliferation. The number of stromal cells was 7% of the total cell population, which is the quantity necessary for tissue compaction. A suspension of 1.3×10^6 cells within reconstitution mixture containing 2.25 mg/mL collagen I (BD Biosciences) and 0.5 mg/mL human fibrinogen (Sigma) was added to the substrate. We measured CMT function at day 7 to allow for tissue compaction and stability of force generation. For quantifying tissue forces, fluorescence images were taken at 25 Hz with an Andor Dragonfly microscope (Andor iXon 888 EMCCD camera with HC PL Fluotar 5 \times objective mounted on a DMI8 [Leica] microscope that was equipped with a fully enclosed live-cell environmental chamber [Okolabs]). All tissues were biphasic stimulated at 1 Hz with a C-Pace EP stimulator (IonOptix) and platinum wire electrodes that were separated by 2 cm to the sides of the tissues tested. The displacement of fluorescent microbeads was tracked using the ParticleTracker plug-in in ImageJ (NIH). Displacement values were analyzed in Excel (Microsoft) to compute twitch force (dynamic force), resting tension, and kinetics. Resting tension was measured by subtracting the resting cantilever position from the cantilever position prior to tissue generation. Cantilever spring constants were computed using the empirically determined elastic modulus of PDMS and the dimensions of the tissue gauge device as described previously (Boudou et al., 2012). For small-molecule treatment, CMTs were treated in Tyrode's solution for 10 min with verapamil (Tocris), blebbistatin (Tocris), pifithrin- α (Tocris), or NAC (Sigma) prior to force measurements.

ACCESSION NUMBERS

Analyzed data are provided in supplemental tables. Genome sequencing datasets are deposited at the GEO under accession number GEO: GSE113907.

SUPPLEMENTAL INFORMATION

Supplemental Information includes Supplemental Experimental Procedures, five figures, five tables, and two videos and can be

found with this article online at <https://doi.org/10.1016/j.stemcr.2018.11.015>.

AUTHOR CONTRIBUTIONS

R.C., K.T., A.L., F.L., A.M.P., R.R., E.M., Y.-S.C., and J.T.H. designed and performed iPSC and iCM research, and analyzed and interpreted data. R.C., K.T., and J.T.H. wrote the manuscript. R.C. designed and engineered cardiac tissue devices. A.L., F.L., A.M.P., R.R., K.T., and R.C. generated cells for this study. K.A. and B.D.H. performed atomic force microscopy analysis of PDMS devices.

ACKNOWLEDGMENTS

We thank Anthony Carcio for contributions to the flow cytometry experiments, and Qianru Yu for expertise in confocal microscopy. We also thank Bo Reese for RNA sequencing technical expertise. We thank Samantha Harris for her generous contribution of MYBPC3 antibody. Funding for this work was supported by the National Heart, Lung, and Blood Institute at the NIH (J.T.H. HL125807 and HL142787).

Received: October 30, 2018

Revised: November 18, 2018

Accepted: November 19, 2018

Published: December 13, 2018

REFERENCES

- Ashrafian, H., McKenna, W.J., and Watkins, H. (2011). Disease pathways and novel therapeutic targets in hypertrophic cardiomyopathy. *Circ. Res.* 109, 86–96.
- Blankenburg, R., Hackert, K., Wurster, S., Deenen, R., Seidman, J.G., Seidman, C.E., Lohse, M.J., and Schmitt, J.P. (2014). β -Myosin heavy chain variant Val606Met causes very mild hypertrophic cardiomyopathy in mice, but exacerbates HCM phenotypes in mice carrying other HCM mutations. *Circ. Res.* 115, 227–237.
- Boudou, T., Legant, W.R., Mu, A., Borochin, M.A., Thavandiran, N., Radisic, M., Zandstra, P.W., Epstein, J.A., Margulies, K.B., and Chen, C.S. (2012). A microfabricated platform to measure and manipulate the mechanics of engineered cardiac microtissues. *Tissue Eng. Part A* 18, 910–919.
- Bulkley, B.H., Weisfeldt, M.L., and Hutchins, G.M. (1977). Asymmetric septal hypertrophy and myocardial fiber disarray. Features of normal, developing, and malformed hearts. *Circulation* 56, 292–298.
- Chuan, P., Sivaramakrishnan, S., Ashley, E.A., and Spudich, J.A. (2012). Cell-intrinsic functional effects of the alpha-cardiac myosin Arg-403-Gln mutation in familial hypertrophic cardiomyopathy. *Biophys. J.* 102, 2782–2790.
- Crilly, J.G., Boehm, E.A., Blair, E., Rajagopalan, B., Blamire, A.M., Styles, P., McKenna, W.J., Ostman-Smith, I., Clarke, K., and Watkins, H. (2003). Hypertrophic cardiomyopathy due to sarcomeric gene mutations is characterized by impaired energy metabolism irrespective of the degree of hypertrophy. *J. Am. Coll. Cardiol.* 41, 1776–1782.
- Davis, J., Davis, L.C., Correll, R.N., Makarewich, C.A., Schwane-kamp, J.A., Moussavi-Harami, F., Wang, D., York, A.J., Wu, H.,



- Houser, S.R., et al. (2016). A tension-based model distinguishes hypertrophic versus dilated cardiomyopathy. *Cell* 165, 1147–1159.
- Endoh, M., and Blinks, J.R. (1988). Actions of sympathomimetic amines on the Ca^{2+} transients and contractions of rabbit myocardium: reciprocal changes in myofibrillar responsiveness to Ca^{2+} mediated through alpha- and beta-adrenoceptors. *Circ. Res.* 62, 247–265.
- Fujii, T., and Namba, K. (2017). Structure of actomyosin rigour complex at 5.2 Å resolution and insights into the ATPase cycle mechanism. *Nat. Commun.* 8, 13969.
- Geisterfer-Lowrance, A.A., Kass, S., Tanigawa, G., Vosberg, H.P., McKenna, W., Seidman, C.E., and Seidman, J.G. (1990). A molecular basis for familial hypertrophic cardiomyopathy: a beta cardiac myosin heavy chain gene missense mutation. *Cell* 62, 999–1006.
- Geisterfer-Lowrance, A.A., Christe, M., Conner, D.A., Ingwall, J.S., Schoen, F.J., Seidman, C.E., and Seidman, J.G. (1996). A mouse model of familial hypertrophic cardiomyopathy. *Science* 272, 731–734.
- Gersh, B.J., Maron, B.J., Bonow, R.O., Dearani, J.A., Fifer, M.A., Link, M.S., Naidu, S.S., Nishimura, R.A., Ommen, S.R., Rakowski, H., et al. (2011a). 2011 ACCF/AHA guideline for the diagnosis and treatment of hypertrophic cardiomyopathy: a report of the American College of Cardiology Foundation/American Heart Association Task Force on practice guidelines. *Circulation* 124, e783–e831.
- Gersh, B.J., Maron, B.J., Bonow, R.O., Dearani, J.A., Fifer, M.A., Link, M.S., Naidu, S.S., Nishimura, R.A., Ommen, S.R., Rakowski, H., et al. (2011b). 2011 ACCF/AHA guideline for the diagnosis and treatment of hypertrophic cardiomyopathy: executive summary: a report of the American College of Cardiology Foundation/American Heart Association Task Force on practice guidelines. *Circulation* 124, 2761–2796.
- Han, J., Flemington, C., Houghton, A.B., Gu, Z., Zambetti, G.P., Lutz, R.J., Zhu, L., and Chittenden, T. (2001). Expression of *bbc3*, a pro-apoptotic BH3-only gene, is regulated by diverse cell death and survival signals. *Proc. Natl. Acad. Sci. U S A* 98, 11318–11323.
- Hinson, J.T., Chopra, A., Nafissi, N., Polacheck, W.J., Benson, C.C., Swist, S., Gorham, J., Yang, L., Schafer, S., Sheng, C.C., et al. (2015). HEART DISEASE. Titin mutations in iPS cells define sarcomere insufficiency as a cause of dilated cardiomyopathy. *Science* 349, 982–986.
- Hinson, J.T., Chopra, A., Lowe, A., Sheng, C.C., Gupta, R.M., Kuppusamy, R., O'Sullivan, J., Rowe, G., Wakimoto, H., Gorham, J., et al. (2016). Integrative analysis of PRKAG2 cardiomyopathy iPS and microtissue models identifies AMPK as a regulator of metabolism, survival, and fibrosis. *Cell Rep.* 17, 3292–3304.
- Ho, C.Y., Sweitzer, N.K., McDonough, B., Maron, B.J., Casey, S.A., Seidman, J.G., Seidman, C.E., and Solomon, S.D. (2002). Assessment of diastolic function with Doppler tissue imaging to predict genotype in preclinical hypertrophic cardiomyopathy. *Circulation* 105, 2992–2997.
- Ho, C.Y., Day, S.M., Colan, S.D., Russell, M.W., Towbin, J.A., Sheridan, M.V., Canter, C.E., Jefferies, J.L., Murphy, A.M., Cirino, A.L., et al. (2017). The burden of early phenotypes and the influence of wall thickness in hypertrophic cardiomyopathy mutation carriers: findings from the HCMNet study. *JAMA Cardiol.* 2, 419–428.
- Hunten, S., Kaller, M., Drepper, F., Oeljeklaus, S., Bonfert, T., Erhard, F., Dueck, A., Eichner, N., Friedel, C.C., Meister, G., et al. (2015). p53-regulated networks of protein, mRNA, miRNA, and lncRNA expression revealed by integrated pulsed stable isotope labeling with amino acids in cell culture (pSILAC) and next generation sequencing (NGS) analyses. *Mol. Cell. Proteomics* 14, 2609–2629.
- Hwang, P.M., Bunz, F., Yu, J., Rago, C., Chan, T.A., Murphy, M.P., Kelso, G.F., Smith, R.A., Kinzler, K.W., and Vogelstein, B. (2001). Ferredoxin reductase affects p53-dependent, 5-fluorouracil-induced apoptosis in colorectal cancer cells. *Nat. Med.* 7, 1111–1117.
- Jones, R.G., Plas, D.R., Kubek, S., Buzzai, M., Mu, J., Xu, Y., Birnbaum, M.J., and Thompson, C.B. (2005). AMP-activated protein kinase induces a p53-dependent metabolic checkpoint. *Mol. Cell* 18, 283–293.
- Jung, W.I., Sieverding, L., Breuer, J., Hoess, T., Widmaier, S., Schmidt, O., Bunse, M., van Erckelens, F., Apitz, J., Lutz, O., et al. (1998). ^{31}P NMR spectroscopy detects metabolic abnormalities in asymptomatic patients with hypertrophic cardiomyopathy. *Circulation* 97, 2536–2542.
- Kim, S.J., Iizuka, K., Kelly, R.A., Geng, Y.J., Bishop, S.P., Yang, G., Kudej, A., McConnell, B.K., Seidman, C.E., Seidman, J.G., et al. (1999). An alpha-cardiac myosin heavy chain gene mutation impairs contraction and relaxation function of cardiac myocytes. *Am. J. Physiol.* 276, H1780–H1787.
- Kovacs, M., Toth, J., Hetenyi, C., Malnasi-Csizmadia, A., and Sellers, J.R. (2004). Mechanism of blebbistatin inhibition of myosin II. *J. Biol. Chem.* 279, 35557–35563.
- Lakin, N.D., and Jackson, S.P. (1999). Regulation of p53 in response to DNA damage. *Oncogene* 18, 7644–7655.
- Lan, F., Lee, A.S., Liang, P., Sanchez-Freire, V., Nguyen, P.K., Wang, L., Han, L., Yen, M., Wang, Y., Sun, N., et al. (2013). Abnormal calcium handling properties underlie familial hypertrophic cardiomyopathy pathology in patient-specific induced pluripotent stem cells. *Cell Stem Cell* 12, 101–113.
- Lian, X., Zhang, J., Azarin, S.M., Zhu, K., Hazeltine, L.B., Bao, X., Hsiao, C., Kamp, T.J., and Palecek, S.P. (2013). Directed cardiomyocyte differentiation from human pluripotent stem cells by modulating Wnt/ β -catenin signaling under fully defined conditions. *Nat. Protoc.* 8, 162–175.
- Mak, T.W., Hauck, L., Grothe, D., and Billia, F. (2017). p53 regulates the cardiac transcriptome. *Proc. Natl. Acad. Sci. U S A* 114, 2331–2336.
- Malik, F.I., Hartman, J.J., Elias, K.A., Morgan, B.P., Rodriguez, H., Brejc, K., Anderson, R.L., Sueoka, S.H., Lee, K.H., Finer, J.T., et al. (2011). Cardiac myosin activation: a potential therapeutic approach for systolic heart failure. *Science* 331, 1439–1443.
- Marian, A.J., Mares, A., Jr., Kelly, D.P., Yu, Q.T., Abchee, A.B., Hill, R., and Roberts, R. (1995). Sudden cardiac death in hypertrophic cardiomyopathy. Variability in phenotypic expression of beta-myosin heavy chain mutations. *Eur. Heart J.* 16, 368–376.
- Maron, B.J., Gardin, J.M., Flack, J.M., Gidding, S.S., Kurosaki, T.T., and Bild, D.E. (1995). Prevalence of hypertrophic cardiomyopathy



in a general population of young adults. Echocardiographic analysis of 4111 subjects in the CARDIA study. Coronary artery risk development in (young) adults. *Circulation* 92, 785–789.

Maron, B.J., Maron, M.S., and Semsarian, C. (2012). Genetics of hypertrophic cardiomyopathy after 20 years: clinical perspectives. *J. Am. Coll. Cardiol.* 60, 705–715.

Nag, S., Sommesse, R.F., Ujfalusi, Z., Combs, A., Langer, S., Sutton, S., Leinwand, L.A., Geeves, M.A., Ruppel, K.M., and Spudich, J.A. (2015). Contractility parameters of human beta-cardiac myosin with the hypertrophic cardiomyopathy mutation R403Q show loss of motor function. *Sci. Adv.* 1, e1500511.

Nag, S., Trivedi, D.V., Sarkar, S.S., Adhikari, A.S., Sunitha, M.S., Sutton, S., Ruppel, K.M., and Spudich, J.A. (2017). The myosin mesa and the basis of hypercontractility caused by hypertrophic cardiomyopathy mutations. *Nat. Struct. Mol. Biol.* 24, 525–533.

Planelles-Herrero, V.J., Hartman, J.J., Robert-Paganin, J., Malik, F.I., and Houdusse, A. (2017). Mechanistic and structural basis for activation of cardiac myosin force production by omecamtiv mecarbil. *Nat. Commun.* 8, 190.

Saltzman, A.J., Mancini-DiNardo, D., Li, C., Chung, W.K., Ho, C.Y., Hurst, S., Wynn, J., Care, M., Hamilton, R.M., Seidman, G.W., et al. (2010). Short communication: the cardiac myosin binding protein C Arg502Trp mutation: a common cause of hypertrophic cardiomyopathy. *Circ. Res.* 106, 1549–1552.

Sanjana, N.E., Shalem, O., and Zhang, F. (2014). Improved vectors and genome-wide libraries for CRISPR screening. *Nat. Methods* 11, 783–784.

Sen-Chowdhry, S., Jacoby, D., Moon, J.C., and McKenna, W.J. (2016). Update on hypertrophic cardiomyopathy and a guide to the guidelines. *Nat. Rev. Cardiol.* 13, 651–675.

Sommese, R.F., Sung, J., Nag, S., Sutton, S., Deacon, J.C., Choe, E., Leinwand, L.A., Ruppel, K., and Spudich, J.A. (2013). Molecular consequences of the R453C hypertrophic cardiomyopathy mutation on human beta-cardiac myosin motor function. *Proc. Natl. Acad. Sci. U S A* 110, 12607–12612.

Tohyama, S., Hattori, F., Sano, M., Hishiki, T., Nagahata, Y., Matsura, T., Hashimoto, H., Suzuki, T., Yamashita, H., Satoh, Y., et al. (2013). Distinct metabolic flow enables large-scale purification of mouse and human pluripotent stem cell-derived cardiomyocytes. *Cell Stem Cell* 12, 127–137.

Wessels, A., Vermeulen, J.L., Viragh, S., Kalman, F., Lamers, W.H., and Moorman, A.F. (1991). Spatial distribution of "tissue-specific" antigens in the developing human heart and skeletal muscle. II. An immunohistochemical analysis of myosin heavy chain isoform expression patterns in the embryonic heart. *Anat. Rec.* 229, 355–368.

Yang, X., Pabon, L., and Murry, C.E. (2014). Engineering adolescence: maturation of human pluripotent stem cell-derived cardiomyocytes. *Circ. Res.* 114, 511–523.

Zhang, T., Maier, L.S., Dalton, N.D., Miyamoto, S., Ross, J., Jr., Bers, D.M., and Brown, J.H. (2003). The deltaC isoform of CaMKII is activated in cardiac hypertrophy and induces dilated cardiomyopathy and heart failure. *Circ. Res.* 92, 912–919.

Stem Cell Reports, Volume 12

Supplemental Information

A Contraction Stress Model of Hypertrophic Cardiomyopathy due to Sarcomere Mutations

Rachel Cohn, Ketan Thakar, Andre Lowe, Feria A. Ladha, Anthony M. Pettinato, Robert Romano, Emily Meredith, Yu-Sheng Chen, Katherine Atamanuk, Bryan D. Huey, and J. Travis Hinson

Title: A contraction stress model of hypertrophic cardiomyopathy due to sarcomere mutations

Authors: Rachel Cohn M.S.^{1#}, Ketan Thakar Ph.D.^{1#}, Andre Lowe M.S.¹, Ferial Ladha M.S.², Anthony M. Pettinato B.S.², Robert Romano B.S.², Emily Meredith B.A.^{1,2}, Yu-Sheng Chen Ph.D.¹, Katherine Atamanuk B.S.³, Bryan D. Huey Ph.D.⁴ and J. Travis Hinson M.D.^{1,2}

Supplemental Experimental Procedures:

Calcium (Ca²⁺) imaging using Fluo-4 AM and Indo-1 AM

CMTs were loaded with 4 μ M Fluo-4 AM (ThermoFisher) for 60 minutes at 37°C in Tyrode's solution (140 mM NaCl, 5.4 mM KCl, 1mM MgCl₂, 10mM glucose, 1.8 mM CaCl₂ and 10mM HEPES pH 7.4 with NaOH). Following loading, tissues were washed three times in Tyrodes solution. Using a solid-state 50 mW 488 nm laser and GFP filter (emission 525 \pm 50nm), fluorescence intensities (F/F₀) were obtained while pacing tissues at 1 Hz. All images were captured at 30 fps on an Andor Dragonfly multimodal microscope. For each tissue, at least four regions of interest (ROIs) were analyzed for changes in Fluo-4 intensity, with the resting fluorescence value F₀ determined by the average of the first five frames of the video. Background intensity was subtracted from all values. For iCM resting and caffeine-induced calcium quantification, single iCMs were disassociated from monolayer differentiation batches using accutase (ThermoFisher). Disassociated iCMs were loaded with 5 mM Indo-1 AM (ThermoFisher) in Tyrodes solution. iCMs were analyzed using a FACSymphony A5 analyzer (BD Biosciences). After excitation with a 60 mW 355 nm laser, Indo-1 signal ratios were determined using a 450nm dichroic mirror and BUF395 and BUV496 filters. To determine baseline calcium concentration, iCMs were analyzed for 20 seconds and the average Indo-1 ratio was obtained. To determine caffeine-induced calcium levels, a stock of 20 mM caffeine (ThermoFisher) in Tyrodes buffer was subsequently added to reach a 10 mM caffeine concentration, and maximum Indo-1 ratio was determined instantaneously.

Immunofluorescence, protein quantification and sarcomere analysis

Protein lysates obtained from iCMs were solubilized in RIPA buffer followed by western blotting. For analysis of MYBPC3 protein levels, an antibody that recognizes an n-terminal epitope of MYBPC3 protein was generously provided by Samantha Harris(Harris et al., 2002). All other antibodies used for immunoblotting include p53 (DO-7; ThermoFisher), p21 (#2947; Cell Signaling), phospho- and total ERK (#4370 and #4695; Cell Signaling), phospho- and total AKT (#2965 and #4691; Cell Signaling), phospho- and total p38 (#4511 and #8690; Cell Signaling), phospho- and total JNK (#4668 and #9252; Cell Signaling), phospho- and total CAMKII (#12716 and #4436; Cell Signaling), pH2A.X (#9718; Cell Signaling), GAPDH (#5174; Cell Signaling) and TNNI3 (#186820; ThermoFisher). For immunofluorescence, iCMs and CMTs were fixed with 4% paraformaldehyde (PFA) for 10 minutes, permeabilized and stained with antibodies to cardiac alpha actinin (#9465; Abcam) with DAPI co-stain. All immunofluorescence imaging was completed using a solid-state laser confocal microscope (Andor Dragonfly). CMT sarcomere analysis was done according to established methods(Bray et al., 2008). To determine z-disk anisotropy, CMTs were fixed with 4% PFA, permeabilized and immunostained with antibodies directed against Z-disk protein cardiac alpha actinin. Confocal images were obtained and analyzed using a modified ridge detection algorithm in ImageJ (NIH) to produce spatial maps of sarcomere Z-disks and the local orientation with respect to the x-axis of the image. For sarcomere length analysis, CMTs were relaxed in calcium-free buffer, fixed with 4% PFA, permeabilized and immunostained with antibodies directed against Z-disk protein

cardiac alpha actinin. Confocal images were analyzed in ImageJ (NIH) using a Z-disk profile plot of greater than three regions of interest per CMT. ICM cell area was measured in iCMs that were cultured on glass coverslips, fixed with 4% PFA, permeabilized, and similarly immunostained. ICM cell area were measured using ImageJ.

Cell viability, mitochondria and oxidative stress assays

For metabolic stress assays, iCMs were cultured at sub-confluence in 6-well plates coated with fibronectin (10 μ g/ml; Corning) at a density of 100,000 cells/well. Prior to metabolic stress conditions, cells were maintained in RPMI with B27 supplement. To induce nutrient stress, cells were maintained in glucose-free DMEM media (ThermoFisher) with B27 supplement for up to 7 days. To quantify iCM death, either LDH released from dead cells was analyzed from conditioned media using an LDH release assay (ThermoFisher), or viable cells were counted using live-cell imaging and a viability stain (MitoTracker Red CMXRos). ICM conditioned media was analyzed in a 96-well plate with a Synergy plate reader (BioTek) to quantify absorbance at 490 nm and 680 nm. For ADP/ATP ratios, 20,000 iCMs were plated on fibronectin-coated (10 μ g/ml; Corning) 96-well plates and analyzed by a bioluminescent ADP/ATP assay (Biovision). For mitochondrial content and reactive oxygen assays, iCMs were stained with MitoTracker Green (ThermoFisher) or MitoSOX Red (ThermoFisher) in accord with manufacturer's recommendations and single, disassociated iCMs were analyzed by FACS.

RNA sequencing, quantitative PCR and computational analyses

For iCM RNA sequencing experiments, total RNA was isolated from day 30-35 iCMs using Trizol (ThermoFisher). CDNA was constructed using Superscript III First-Strand synthesis (ThermoFisher). For each sample, total RNA from biological triplicates by differentiation batch was collected and sequenced. RNA sequencing libraries were generated using the TruSeq Stranded mRNA library preparation kit (Illumina). RNA sequencing libraries were sequenced on a HiSeq 2500 v4 SBS platform 2x100bp reads (Illumina). Sequences were aligned with STAR(Engstrom et al., 2013) to the hg38 human genome. For differential expression, DESeq2 (Bioconductor) was used. Heatmap analysis and hierarchical clustering were performed using the Morpheus tool (Broad Institute). For quantitative PCR analysis, iCM total RNA was isolated and processed as above. Gene-specific PCR primers were identified from the literature or designed using Primer3 (see table S1 for primer sequences) and transcripts were quantified using Fast SYBR Green (Applied Biosystems) on a ViiA7 Real-Time PCR system (Applied Biosystems). RNA sequencing results files have been deposited in GEO (GSE113907).

AFM Modulus Quantification

To measure the elastic modulus of the PDMS used for tissue gauge production, indentation measurements were performed using Atomic Force Microscopy (AFM) (Asylum Research MFP-3D, Santa Barbara, Ca). Using a colloidal silica spherical probe (AppNano FORT SiO₂-A), a 16x16 array of force-distance curves was acquired evenly spaced across a 2x2 μ m area for each measurement. Before and after these force-volume experiments, identical force-distance measurements on an incompressible surface were performed with a steel disk to calibrate the system sensitivity and to determine the spring constant for the force-transducing cantilever (1.75 nN/nm of deflection, within the range of specifications for these commercial probes). All 256 force-distance curves for each location studied were analyzed based on the Johnson-Kendall-Roberts model of elastic contact. Such JKR mechanics accommodate large adhesion energies between an indenting probe and sample(Gupta et al., 2007; Huey, 2007), both expected and observed for these studies with PDMS. This incorporates the following experimental parameters: the indenter possesses a spherical tip geometry with a radius of 2.5 μ m; the probe modulus

appropriate for the colloidal silica sphere is 68.0 GPa; and this probe exhibits a Poisson ratio of 0.19. A Poisson ratio of .33 is conventionally assumed for the specimen. For each of the samples, force-volume maps were completed at three representative locations. The average elastic modulus from the resulting 768 individual indentations per specimen is reported.

Supplemental Figures:

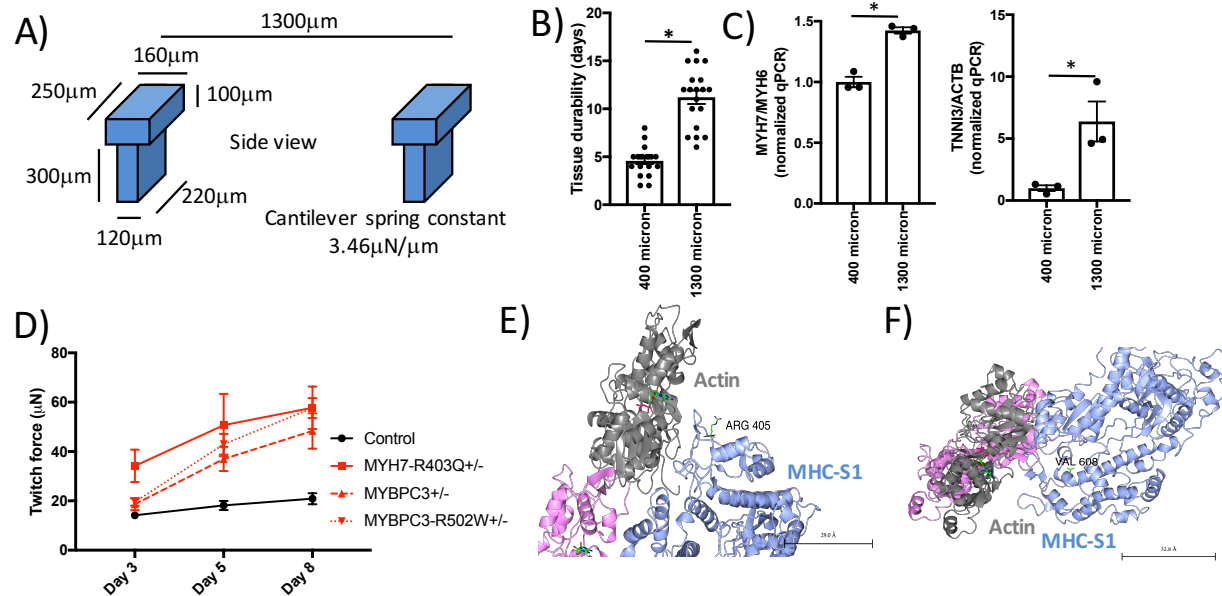


Figure S1. CMT assay to study HCM models. (A) Design of cantilevers is shown with xyz dimensions. (B) New cantilever design and larger CMTs resulted in improved tissue durability as measured by tissue survival. (C) Sarcomere gene expression (left panel-MYH7 normalized to MYH6 and right panel-TNNI3 normalized to ACTB loading control) was measured using quantitative PCR between cDNA libraries produced from tissue samples of 400 µm and 1300 µm size. (D) Maximum twitch force plateaus for CMT models after day 5. (E) Ribbon diagram from electron cryomicroscopy structure of rabbit actomyosin rigor complex (myosin heavy chain S1 (MHC-S1) colored blue and actin monomers colored gray and pink) showing location of R403Q (equivalent to R405 in rabbit MHC)(Fujii and Namba, 2017). (F) Ribbon diagram from electron cryomicroscopy structure of rabbit actomyosin rigor complex showing location of V606M (equivalent to V608 in rabbit MHC)(Fujii and Namba, 2017). Significance was assessed by Student's t-test (B, C; *all $p < 0.05$); data are means \pm SEM (error bars) (B, C and D). Scale bars are 29Å (E) and 32.8Å (F). Each data point represents a single CMT (B) or a sample generated from a batch of CMTs (C, D) produced by at least three biological replicates by iPS differentiation batch.

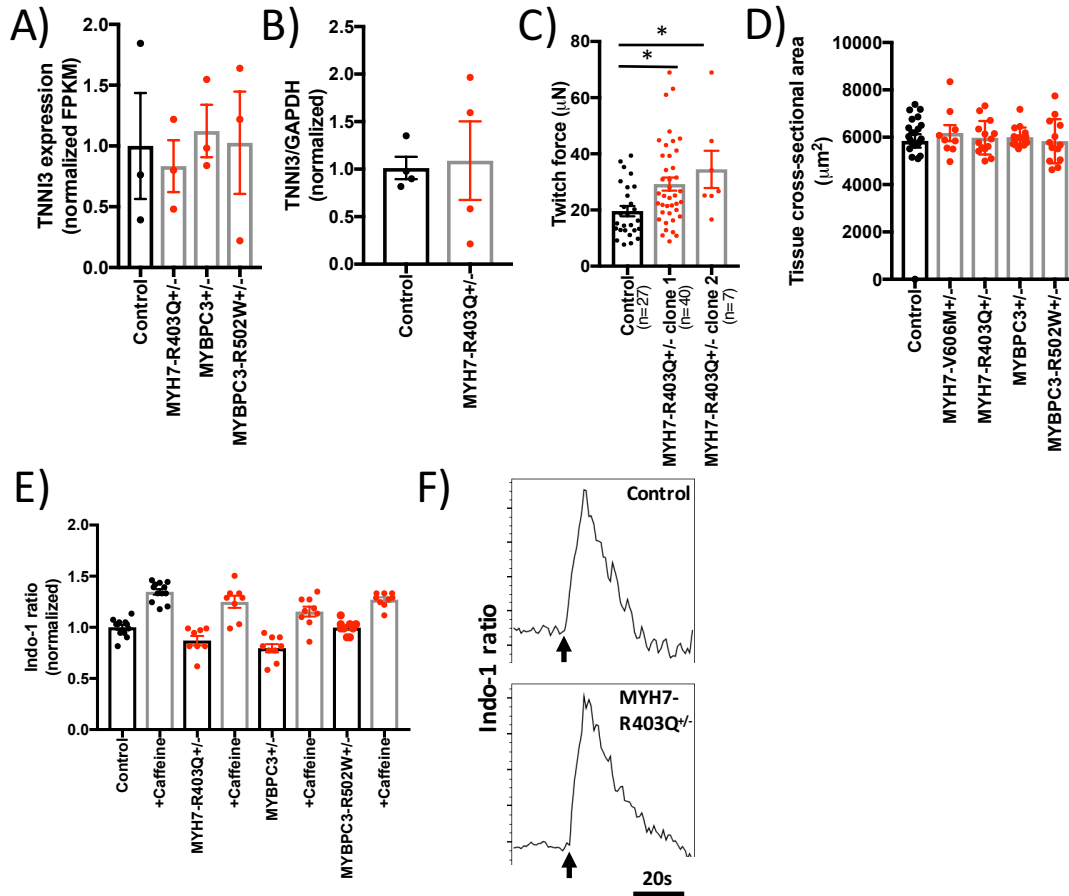


Figure S2. Characterization of HCM CMT models. (A) *TNNI3* normalized expression by RNA sequencing. (B) *TNNI3* protein levels quantified by immunoblotting and densitometry analysis and normalized to GAPDH. (C) Maximum twitch force of CMTs generated from two independent clones of MYH7-R403Q^{+/-} compared to isogenic controls. (D) Tissue cross-sectional area measured by confocal microscopy of four HCM models compared to isogenic controls. (E) Normalized basal and caffeine-induced calcium levels using FACS analysis to quantify Indo-1 ratiometric signal for HCM and control iCMs. (F) Representative FACS tracing of Indo-1 ratiometric signal for isogenic control or MYH7-R403Q^{+/-} iCMs (black arrow denotes time of caffeine stimulation). Significance (*p<0.05 and **p<0.001) was assessed by FDR (A), Student's t-test (B) or ANOVA (A, C, D, and E); data are means \pm SEM (error bars) (A-E). Each data point represents a sample generated from a batch of CMTs (A, B) or a single CMT (C-E) produced by at least three biological replicates by iPS differentiation batch.

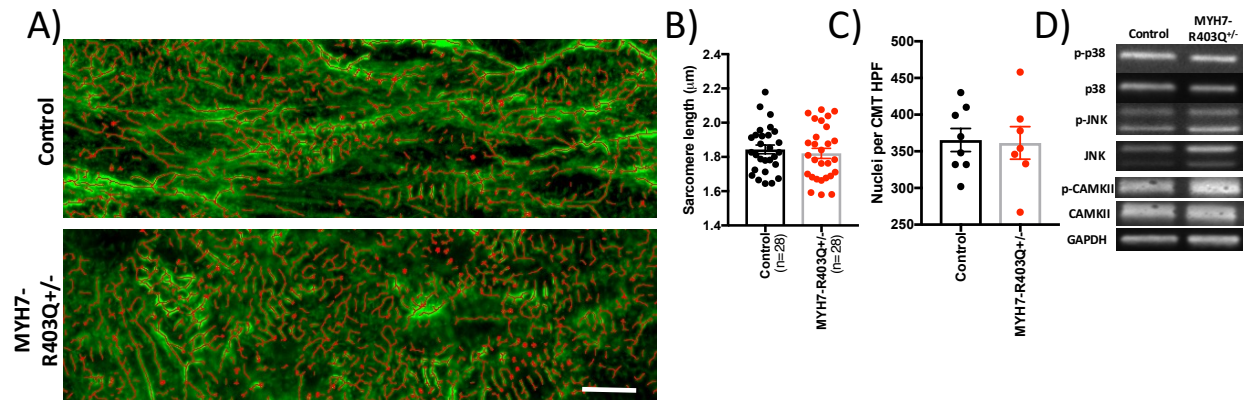


Figure S3. Sarcomere structure and functional analysis of HCM CMTs and iCMs. (A) Representative images of fixed CMTs immunostained with antibodies to cardiac alpha actinin to decorate sarcomere Z-disks (green) and analyzed by a modified ridge detection algorithm. Representative ridges shown in red with overlay confocal images (scale bar=10 μm). (B) Average sarcomere length obtained from confocal images of relaxed CMTs stained with antibodies to cardiac alpha actinin to decorate Z-disks. (C) CMT nuclei per high power field (HPF) of CMTs was quantified using confocal images of DAPI stained tissues. (D) Representative immunoblots from MYH7-R403Q^{+/−} and control iCM lysates probed with antibodies to phospho- and total p38, phospho- and total JNK, phospho- and total CAMKII as well as GAPDH (loading control). Significance was assessed by Student's t-test (B and C); data are means \pm SEM (error bars) (B and C). Each data point represents a sample generated from a single CMT (B, C) produced by at least three biological replicates by iPS differentiation batch.

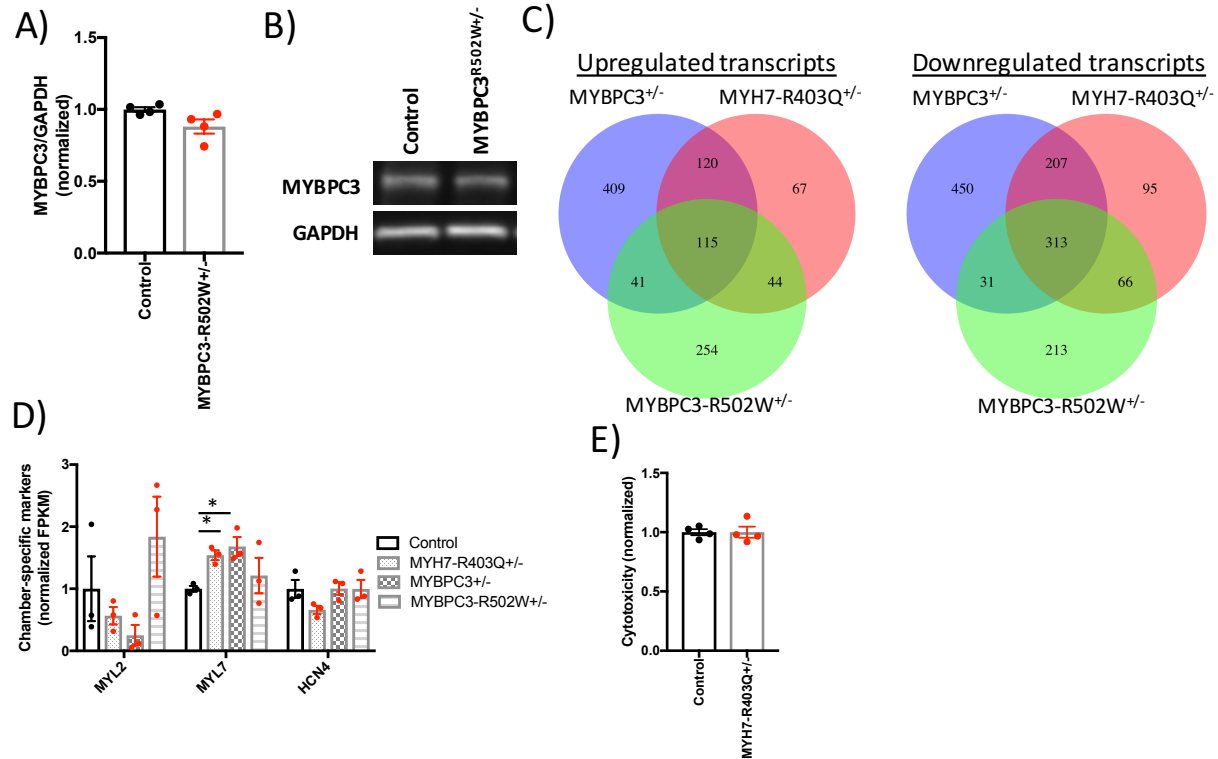


Figure S4. RNA sequencing of HCM models. (A) Quantification of MYBPC3 protein levels normalized to GAPDH by densitometry analysis of immunoblots of iCM lysates. (B) Representative MYBPC3 and GAPDH immunoblot used for (A). (C) Venn diagram to illustrate overlap in differential gene expression from RNA sequencing data obtained from three HCM models compared to isogenic controls (all FDR<0.10; log₂FC>0.3 or <-0.3; see table S4). (D) Transcript levels of cardiac chamber-specific genes as quantified by RNA sequencing. (E) Cytotoxicity of iCMs cultured in growth media. Significance (p<0.05) was assessed by Student's t-test (A, E) or FDR (C-D); data are means +/- SEM (error bars) (A, D and E). Each data point represents a sample generated from a batch of CMTs (A, C, D, E) produced by at least three biological replicates by iPS differentiation batch.

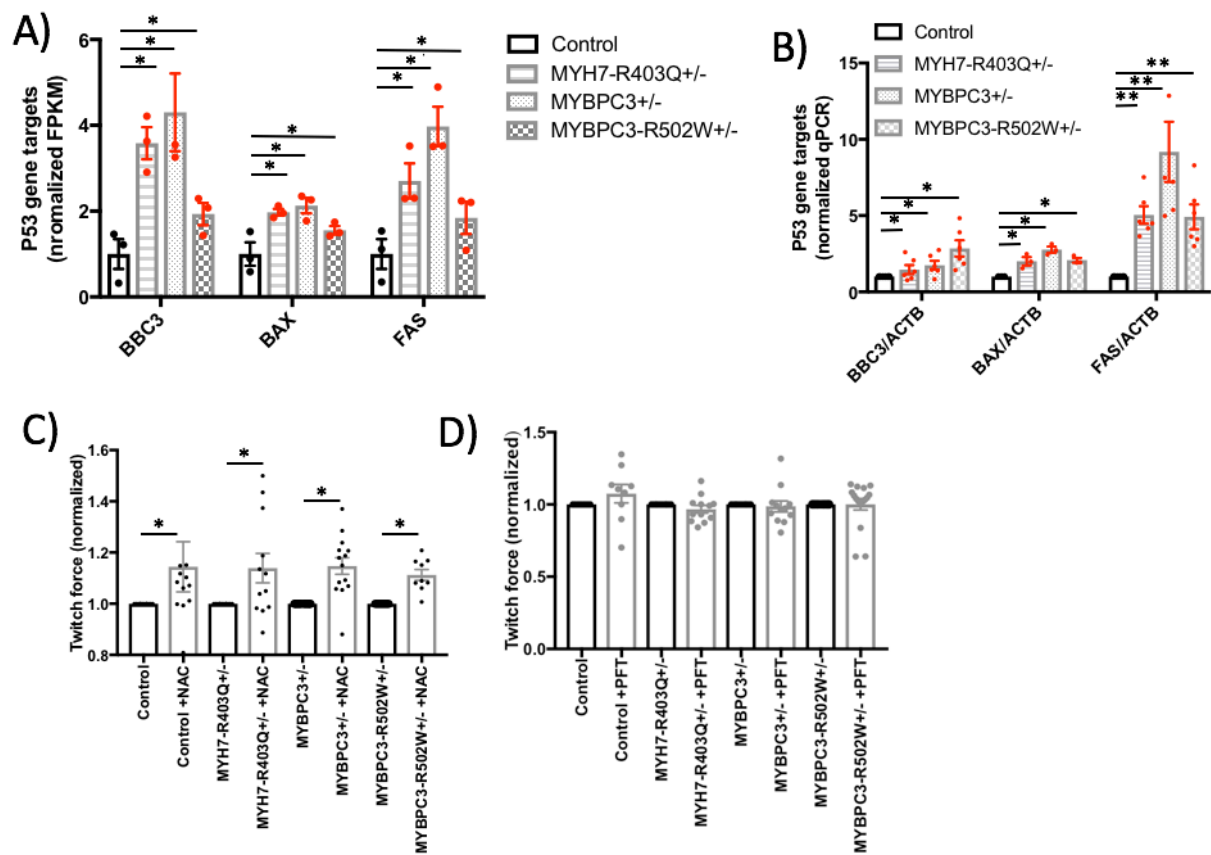


Figure S5. CMT force production after inhibition of p53 or oxidative stress using small molecules. (A) RNA-seq and (B) quantitative PCR analysis of p53 transcriptional targets in HCM compared to isogenic control iCMs. (C) Quantification of CMT twitch force after treatment with N-acetyl cysteine (NAC) compared to carrier control for HCM iCMs and isogenic controls. (D) Quantification of CMT twitch force after treatment with p53 inhibitor pifithrin- α (PFT) compared to carrier control for HCM iCMs and isogenic controls. Significance (* $p < 0.05$) was assessed by FDR (A), ANOVA (B) and Student's t-test (C), and data are means \pm SEM (error bars) (A-C). Each data point represents a sample generated from a batch of CMTs (A, B) or a single CMT (C, D) produced by at least three biological replicates by iPS differentiation batch.

Captions for Tables S1-S5

Table S1. CRISPR, PCR and other oligo sequences. (A) Sequences for gRNA backbone, mutation-specific gRNA recognition site, ssODN HR donor sequence and Sanger sequencing primers for genome engineering experiments involving the *MYH7* and *MYBPC3* genes. (B) Summary statistics of CRISPR/Cas9 genome editing efficiencies in HCM iPS models including homology-directed repair (HDR) and non-homology end-joining (NHEJ) repair efficiencies. (C) LentiCRISPR experiments targeting *TP53* in iCMs including all gRNA sequences, oligonucleotides and qPCR primers for all gene expression studies.

Table S2. CRISPR off-target and iPSc CNV results. (A) List of *in silico* off-target CRISPR genomic loci that were predicted by crispr.mit.edu and sequencing primers to verify genotypes. (B) iPSc CNV analysis by virtual karyotyping using SNP arrays.

Table S3. Principle components from iCM RNA sequencing. Gene components and expression levels (fragments per million) of principle components 1 and 2 from fig.5D, E.

Table S4. Differential expression from iCM RNA sequencing. Upregulated and downregulated gene transcripts from DESeq2 analysis of biological triplicates from *MYBPC3*^{+/-}, *MYBPC3-R502W*^{+/-} and *MYH7-R403Q*^{+/-} compared to isogenic controls and organized by log₂ fold change (>0.3 or <-0.3) and adjusted p-value (FDR cutoff <0.1).

Table S5. Pathway analysis from iCM RNA sequencing. Pathways enriched by Ingenuity Pathway Analysis of differential gene expression in HCM models compared to isogenic controls.

Captions for Movies S1-S2

Movie S1. Isogenic control CMT paced at 1Hz. Magnification- 5X. Scale bar=250µm.

Movie S2. HCM (*MYBPC3-R502W*^{+/-}) CMT paced at 1Hz. Magnification- 5X. Scale bar=250µm.

Supplemental references:

Bray, M.A., Sheehy, S.P., and Parker, K.K. (2008). Sarcomere alignment is regulated by myocyte shape. *Cell Motil Cytoskeleton* 65, 641-651.

Engstrom, P.G., Steijger, T., Sipos, B., Grant, G.R., Kahles, A., Ratsch, G., Goldman, N., Hubbard, T.J., Harrow, J., Guigo, R., *et al.* (2013). Systematic evaluation of spliced alignment programs for RNA-seq data. *Nat Methods* 10, 1185-1191.

Fujii, T., and Namba, K. (2017). Structure of actomyosin rigour complex at 5.2 Å resolution and insights into the ATPase cycle mechanism. *Nat Commun* 8, 13969.

Gupta, S., Carrillo, F., Li, C., Pruitt, L., and Puttlitz, C. (2007). Adhesive forces significantly affect elastic modulus determination of soft polymeric materials in nanoindentation. *Materials Letters* 61, 448-451.

Harris, S.P., Bartley, C.R., Hacker, T.A., McDonald, K.S., Douglas, P.S., Greaser, M.L., Powers, P.A., and Moss, R.L. (2002). Hypertrophic cardiomyopathy in cardiac myosin binding protein-C knockout mice. *Circ Res* 90, 594-601.

Huey, B.D. (2007). AFM and Acoustics: Fast, Quantitative Nanomechanical Mapping. *Annual Review of Materials Research* 37, 351-385.